Topological electride of t-YCl

Yiwei Liang [1], Xinyan Lin,[2] Biao Wan,[3] Zhaopeng Guo,[2] Xuyan Cao,[1] Dexi Shao,[2,*] Jian Sun,[4,5,†] and Huiyang Gou[1,‡]

[1]*Center for High Pressure Science & Technology Advanced Research, Beijing 100193, China*
[2]*School of Physics, Hangzhou Normal University, Hangzhou 311121, China*
[3]*Key Laboratory of Materials Physics of Ministry of Education, School of Physics and Laboratory of Zhongyuan Light,
Zhengzhou University, Zhengzhou 450052, China*
[4]*National Laboratory of Solid State Microstructures and School of Physics, Nanjing University, Nanjing 210093, China*
[5]*Collaborative Innovation Center of Advanced Microstructures, Nanjing 210093, China*

Topological electrides have attracted extensive attention, not only serving as good platforms for studying Dirac fermion, Weyl fermion, and diverse quasiparticles beyond the Dirac and Weyl fermions, but also hosting rich physical and chemical properties such as low work function, high conductivity, and high electron mobility. Motivated by the synthesized YCl and Y_2Cl_3 electrides with nontrivial topology, we have explored the Y-Cl binary system under pressure. Based on the first-principles calculations and crystal-structure prediction techniques, we find a t-YCl phase with the space group of $P4/nmm$ that is both thermodynamically and lattice dynamically stable, and also recoverable to the ambient condition. Based on the $\boldsymbol{k} \cdot \boldsymbol{p}$ method and irreducible representation analyses, we propose that t-YCl has a topological nodal chain surrounding the Z point in the Brillouin zone without spin-orbit coupling (SOC), and evolves into a Dirac semimetal phase with two Dirac points protected by R_{4z} symmetry when taking SOC into consideration. In addition, based on the band representation (BR) analyses, we find the highest occupied bands belong to $A1@2a$ BR. Since both the Y and Cl atoms occupy the 2c Wyckoff positions, i.e., no atom in t-YCl system locates at the 2a Wyckoff positions, it thus suggests the unconventional nature of an uncompensated state at the 2a Wyckoff position. Remembering the ionic compound nature, the unconventional t-YCl phase hosts great potential to be an electride material, which has been further verified by our electron localization function calculations, with the uncompensated state at 2a Wyckoff position contributed by the interstitial quasiatoms. Our work provides a good theoretical and experimental platform for the study of pressure-induced topological electride states.

I. INTRODUCTION

Since the proposals of Weyl and Dirac semimetals [1–4], topological semimetals (TSMs) have been at the forefront of condensed-matter physics. Unlike topological insulators, topological semimetals exhibit band crossings near the Fermi level. It is beneficial to the study of various quasiparticles in condensed-matter physics. Depending on the nodal dimensions (denote as "d") and configurations, many TSMs have been proposed and classified, such as Weyl semimetals [1,5–15], Dirac semimetals [2,3,16–22] for $d = 0$, node-line semimetals [23–26], nodal-chain semimetals [27–31] for $d = 1$, and many other semimetals with unconventional quasiparticles beyond Dirac and Weyl fermions [32]. These findings have greatly improved our understanding of gapless topological phases.

In addition, electrides are a special class of materials in which not all the electrons are bounded around the corresponding atoms, with extra electrons present in the interspace between cations. The interspace occupied with extra electrons behaves as an anion and is therefore also called an interstitial quasiatom (ISQ) [33–35], whose electronic charge centers do not match the real atomic positions. It has been widely used in high-performance catalysts, electron emitters, spintronic devices, nonlinear optics, high-pressure superconductors, high electron mobility carriers, ion batteries, low-temperature superconductivity [36–41] field, etc. Due to the lack of strong confinement in ISQs [42–44], electrides tend to exhibit high electron mobility, low work function [45,46], and floating bands close to Fermi level (E_F) [47]. Due to the fascinating physical properties and prospects of the electride and topological materials, topological electride materials hosting ISQs and topological nontrivial band structures have aroused great interest in materials field. However, although a large number of TSMs and electride materials have been proposed, few electrides with nontrivial TSM phase have been proposed. According to the topological quantum chemistry (TQC), most of the TSM phases can be deduced from the compatibility

*Corresponding author: sdx@hznu.edu.cn
†Corresponding author: jiansun@nju.edu.cn
‡Corresponding author: huiyang.gou@hpstar.ac.cn

relations, and simultaneously, the mismatch between the electronic charge centers and the atomic positions in the unconventional materials can be derived from band representation (BR) analyses, which suggests that symmetry analyses (with compatibility relation analyses and BR analyses) are very useful for finding topological electrides.

Since transition metals with d orbitals have the electron-rich nature, which are very important for the construction of electrides, the binary Y-Cl system has great potential in finding topological electride candidates. For example, in the synthesized Y_2Cl_3 and YCl at ambient pressure, the native quasi-1D and 2D electrides have been proposed [48]. Simultaneously, a 2D-electride YCl system was proposed to have nontrivial band topology [49]. In addition, applying pressure is considered as a powerful method to search for and explore more interesting materials [50,51], such as making electrides by squeezing the elections off from the valence shell [52,53]. Thus, in this work, we explore the binary Y-Cl system under pressure from 0 to 100 GPa through MAGUS and CALYPSO methodology and first-principles calculations. Interestingly, a tetragonal YCl (t-YCl) phase with a topologically nontrivial band structure and ISQ appears at 10 GPa. Based on density-functional theory (DFT) calculations and symmetry analysis, we find that t-YCl is a topological nodal-chain semimetal, with two nodal rings touching each other surrounding the Z point. Taking SOC into consideration, the nodal chain disappears, leaving two Dirac points protected by R_{4z}. Thanks to the TQC proposed by Bradlyn $et\ al.$ [54], BR [55] analysis shows that the highest occupied bands belong to $A1@2a$ BR, indicating its unconventional nature. Further DFT calculations of the electron localization function (ELF) confirm the existence of an uncompensated state at 2a Wyckoff positions occupied by zero-dimensional (0D) ISQs with 2.091 e^-. Meanwhile, t-YCl has a low work function (WF) of 2.724 eV on the (1 0 0) surface, which also indicate the loose bound character of delocalized electrons. As a result, the t-YCl is a topological electride whose nontrivial topology is mainly contributed by ISQs. Our work provides a platform for the study of topological electrides.

II. CALCULATION METHOD

The CALYPSO [56,57] codes based on the swarm intelligence structure prediction technique were performed to search the Y-Cl system under pressures from 0 to 100 GPa, and the final results can also be obtained by the MAGUS [58–60] codes. Structural relaxations and electronic structure calculations are based on density-functional theory using the Vienna $Ab\ initio$ Simulations Package (VASP) [61]. The exchange-correlation functional is given by the generalized gradient approximation parametrized by Perdew, Burke, and Ernzerhof [62]. The plane-wave cutoff energy of 500 eV and Monkhorst-Pack k meshes with a grid spacing of $2\pi \times 0.02$ Å^{-1} are adopted to give energy and force convergence precisions of 10^{-6} eV and 10^{-3} eV Å^{-1}, respectively. The dynamic stabilities of the predicted structures were verified by phonon calculations using the direct supercell method with the PHONOPY code [63]. $Ab\ initio$ molecular dynamics (MD) simulations are carried out using the Nosé-Hoover chain thermostat with highest temperature of 2000 for 6 ps with a time step of

1 fs. The work function (Φ_{WF}) of t-YCl considers (1 0 0), (0 0 1), and (1 1 0) surface and constructs the slab models with 56, 40, and 40 atoms perpendicular or parallel to the layer, and vacuum was about 20 Å. Using Gamma scheme, the k-point grides were set as $1 \times 5 \times 2$, $5 \times 5 \times 1$, and $1 \times 3 \times 4$, respectively. The WF value was calculated through the formula of $\Phi_{WF} = E_{vac} - E_F$ (E_{vac} is vacuum level, E_F is Fermi level). The IRVSP [64] and POS2ABR [65] codes were used for the irreducible representations and BR analyses.

III. RESULTS AND DISCUSSION

A. Phase diagram of Y-Cl system

We construct the convex hull of Y-Cl at 0, 50, and 100 GPa, respectively. As presented in Fig. 1(a), our crystal-structure search strategy reproduces the synthesized structures of $I4/mcm$ Y_2Cl, R-$3m$ YCl, and $C2/m$ Y_2Cl_3 and YCl_3. In particular, the metastable R-$3m$ YCl has a rather high positive formation enthalpy, about 48 meV per atom at 0 GPa, which is relatively smaller than that of Yu $et\ al.$ [66] (derived from their convex hull graph, close to 88.7 meV per atom), and the possible reason may be that the effect of magnetism of R-$3m$ YCl is not considered in the calculation. We predict seven structures, which are $Cmcm$ Y_2Cl at 9–11.6 GPa, $P4/mbm$ Y_3Cl_2 at 96–100 GPa, $P4/nmm$ YCl at 10–10.7 GPa, $Cmcm$ YCl above 64.1 GPa, $P2_1/m$ YCl_2 at 8.2–13 GPa, $P2_1/c$ YCl_3 at 45–66.3 GPa, and $Pnma$ YCl_3 above 66.3 GPa. Detailed structural parameters are provided in Supplemental Material [67], Table SI. Some predicted metastable phases with energy differences <5 meV/atom are also summarized in Supplemental Material [67], Table SII.

B. Crystal structures and stability of Y-Cl compound

Y_2Cl is thermodynamically stable starting from 9 GPa, has an orthorhombic structure with a space group of $Cmcm$, and each Cl atom is coordinated with six Y atoms to form a two-dimensional AA stack structure, which is composed of misaligned Y layers enclosing Cl atoms [Fig. 2(a)]. Above 11.6 GPa, it transforms into an energetically favorable tetragonal structure, synthesized at ∼41 GPa and ∼2000 K [68] with a space group of $I4/mcm$, where the Cl atoms now coordinate eight Y atoms, forming a robust 3D framework [Fig. 2(b)]. With the increasing Cl concentration, the 2D high-pressure electride [66] Y_3Cl_2 with space group of R-$3m$ is thermodynamic stable at 10 to 12.1 GPa; the structure has the "AB" stacked Y-Cl-Y-Cl-Y five-story layer and Cl atoms have a longitudinal symmetry in coordination with six Y atoms [Fig. 2(c)]. Above 96 GPa, a thermodynamically stable tetragonal phase appears with a space group of $P4/mbm$; each Cl atom is coordinated with eight Y atoms to form 3D framework [Fig. 2(d)].

For YCl, the thermodynamic stability of t-YCl begins at 10 GPa with a space group of $P4/nmm$, where Cl atoms are coordinated by five Y atoms and are wrapped into a sandwich-like Y-Cl-Cl-Y layer. These thick layers are AA stacked, showed in Fig. 2(e). The stability interval of this structure is very narrow and it will transform into a hexagonal structure of $P6_3/mmc$ at 10.7 GPa, where each atom has six coordination
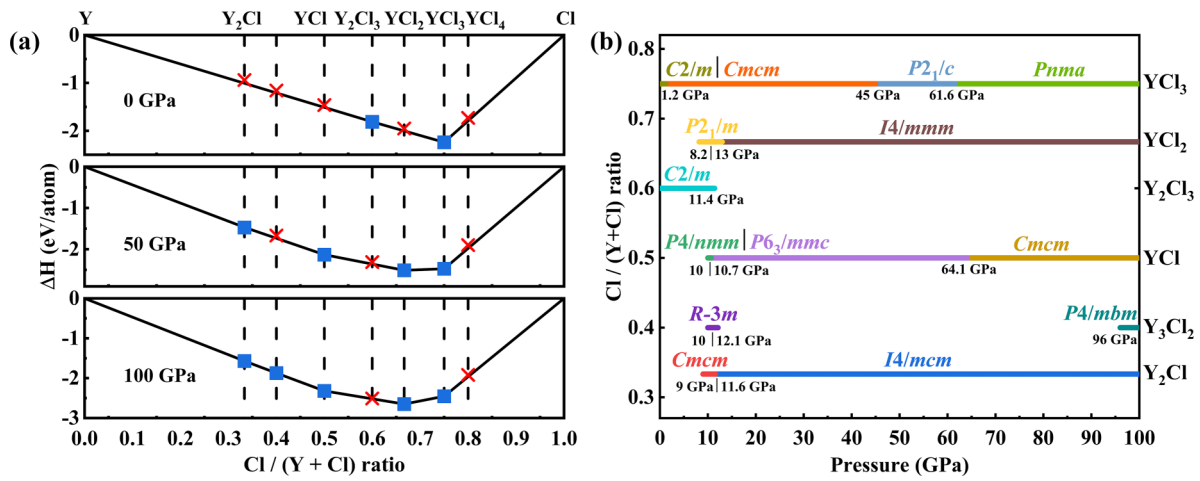
FIG. 1. (a) Calculated convex hull of the Y_xCl_y ($x = 1, 2$ and $y = 1 - 4$) system at 0, 50, and 100 GPa. Thermodynamically stable and metastable stoichiometries are presented as blue squares and red crosses, respectively. (b) Phase diagrams for Y-Cl from 0 to 100 GPa.

to form 3D frame [Fig. 2(f)]. When the pressure increases above 65.1 GPa, the orthorhombic *Cmcm* phase become energetically favorable, and Y atoms insert the seven Cl atoms of the coordination and construct the 3D framework [Fig. 2(g)]. In contrast to YCl, Y_2Cl_3, has a monoclinic structure with a space group of *C2/m* at ambient pressure, synthesized at

1000 K [69], but becomes unstable at 11.4 GPa; it is composed of the layers of chained Y octahedra with Cl "ears" [Fig. 2(h)].

For YCl_2, we find a monoclinic phase with space group $P2_1/m$ at 8.2 GPa, whose framework resembles a stacked twisted chain layer that is connected by Cl atoms [Fig. 2(i)]. When the pressure reaches 13 GPa, it transforms into a tetrag-
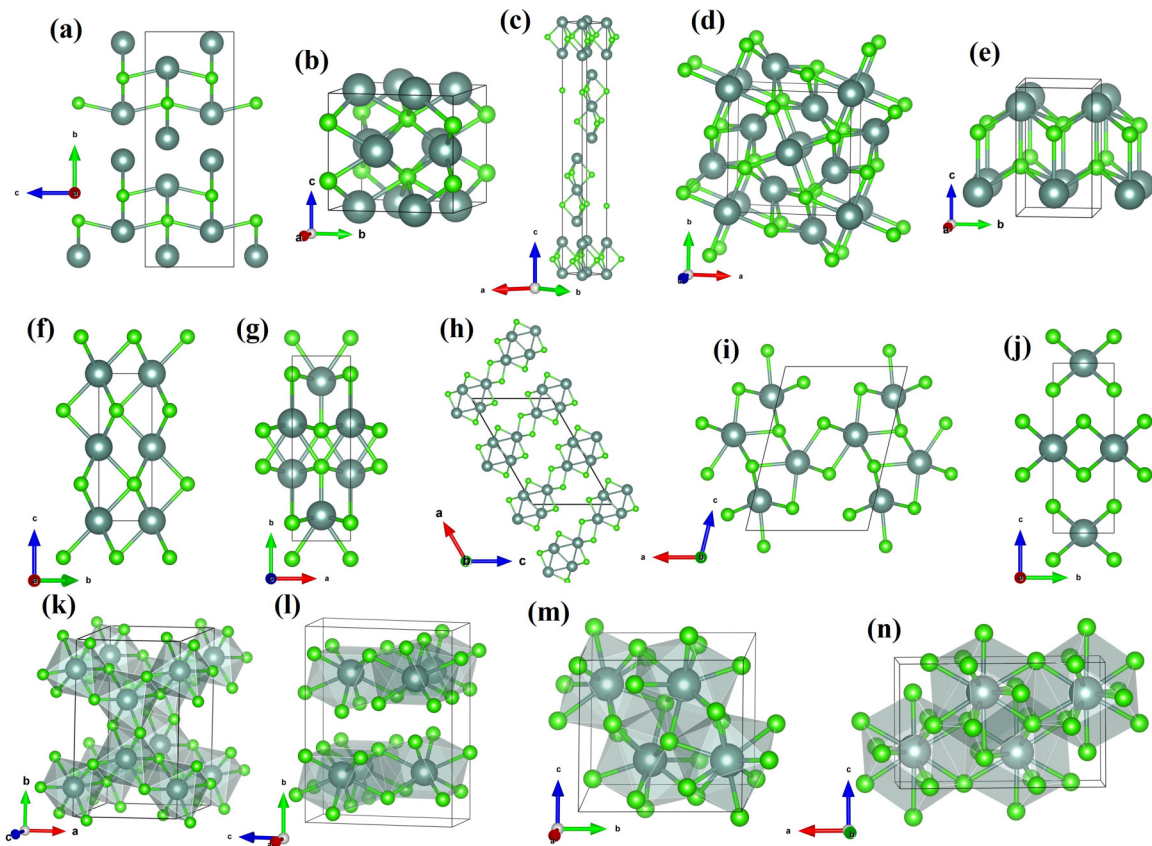

FIG. 2. Crystal structures of (a) *Cmcm* and (b) *I4/mcm* Y_2Cl at 10 and 50 GPa; (c) *R-3m* and (d) *P4/mbm* Y_3Cl_2 at 10 and 100 GPa; (e) *P4/nmm*, (f) $P6_3/mmc$ and (g) *Cmcm* YCl at 10, 20, and 100 GPa; (h) *C2/m* Y_2Cl_3 at 0 GPa; (i) $P2_1/m$ and (j) *I4/mmm* YCl_2 at 10 and 50 GPa; (k) *C2/m*, (l) *Cmcm*, (m) $P2_1/c$ and (n) *Pnma* YCl_3 at 0, 10, 50, and 100 GPa, respectively.
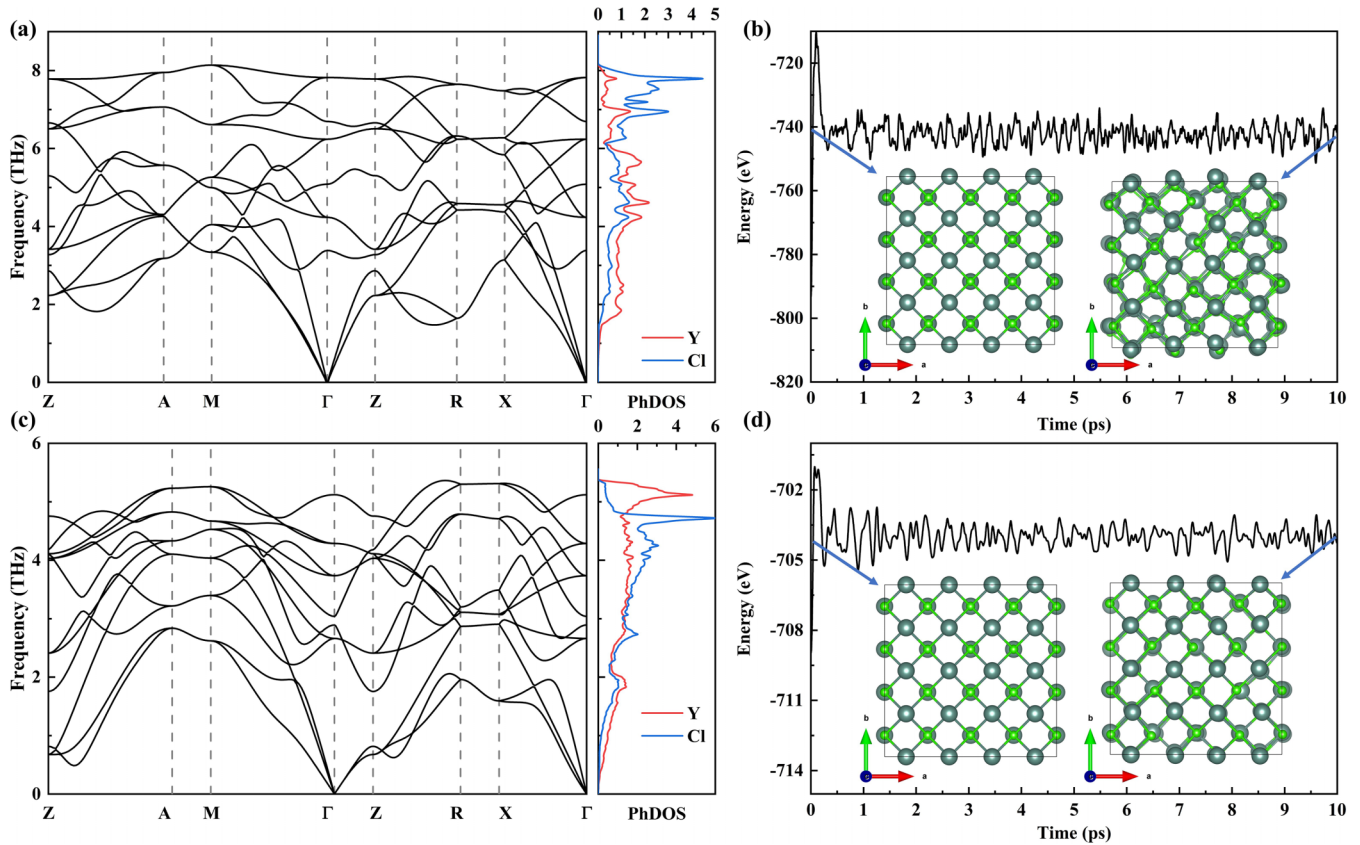
FIG. 3. Phonon dispersions and phonon density of states (PhDOS) for t-YCl at (a) 10 GPa and (c) 0 GPa 300 K. (b), (d) The energy fluctuations in AIMD simulations for t-YCl at 10 GPa 2000 K and 0 GPa 300 K. The insets are snapshots of structures at the original state and final state.

onal phase with a space group of $I4/mmm$, a structure formed by stacking "*ABA*" layers, each Y atom is coordinated with eight Cl atoms to form the Cl-Y-Cl sandwiches [Fig. 2(j)].

The monoclinic YCl$_3$ with a space group of $C2/m$ was synthesized at atmospheric pressure of 680° [70]; *AA* is stacked by a layer of chlorine octahedron connected by edges. Y atom is trapped in an octahedron with the coordination number of 6 [Fig. 2(k)]. According to our calculations, it transforms into an orthorhombic $Cmcm$ phase at 1.2 GPa. Like the $C2/m$ YCl$_3$, it can be seen as a stacked structure, but with an *AB* stacking, consisting of a layer of edges or atoms connected to chlorine decahedra, Y atoms in cage is added to eight coordination [Fig. 2(l)]. When reaching 45 GPa, the phase becomes a monoclinic structure with a space group of $P2_1/c$; in this structure, Y coordination increase to 9, forming the tetrakaidecahedron unit of chlorine. The units are stacked through shared faces or edges to form a three-dimensional framework with interstice [Fig. 2(m)]. Finally, above 61.6 GPa, the phase transforms into an orthorhombic structure with a space group of $Pnma$, and the Y atomic coordination number increases to 12, forming a hexadecahedron stacked with the chlorine through a shared surface [Fig. 2(n)]. This $Pnma$ phase is modulated by a predicted $Pmmn$ structure with the imaginary frequency of phonon spectrum.

In terms of the t-YCl, both Y and Cl atoms occupy the 2c Wyckoff positions of (0.5, 0.0, 0.816 59) and (0.5, 0.0,

0.353 03) at 10 GPa; the Y-Cl distances are 2.793 Å (four along the fold plane) and 2.889 Å (one along the c axis). Phonon spectra calculations confirm the dynamic stability of t-YCl, as there are no imaginary frequencies throughout the Brillouin zone [Fig. 3(a)]. MD simulations show that the structure of t-YCl can withstand temperature up to 2000 K without structural damage [Fig. 3(b)], indicating the high-temperature stability. We also examine the recoverability at ambient conditions; as shown in Figs. 3(c) and 3(d), t-YCl structures can be maintained at 0 GPa and 300 K. At 10 GPa, the superconductivity is estimated based on the Allen-Dynes-modified McMillan equation with a Coulomb pseudopotential of $\mu^* = 0.1$; T_c is close to zero. The dynamical stability of other structures at the corresponding pressure is confirmed by the absence of imaginary frequencies in phonon dispersion (see in Supplemental Material [67], Fig. S1).

C. Topological electronic property and work function

As the band structures without SOC presented in Fig. 4(a), there exists a band inversion near the Z point, forming a band crossing along the $\Gamma-Z$ line. To give more insights of the band inversion and the band crossing near the Z point, we have established an effective Hamiltonian by $\boldsymbol{k} \cdot \boldsymbol{p}$ method. Taking the crystal symmetries and time-reversal symmetric (TRS) into consideration, the effective Hamiltonian can be
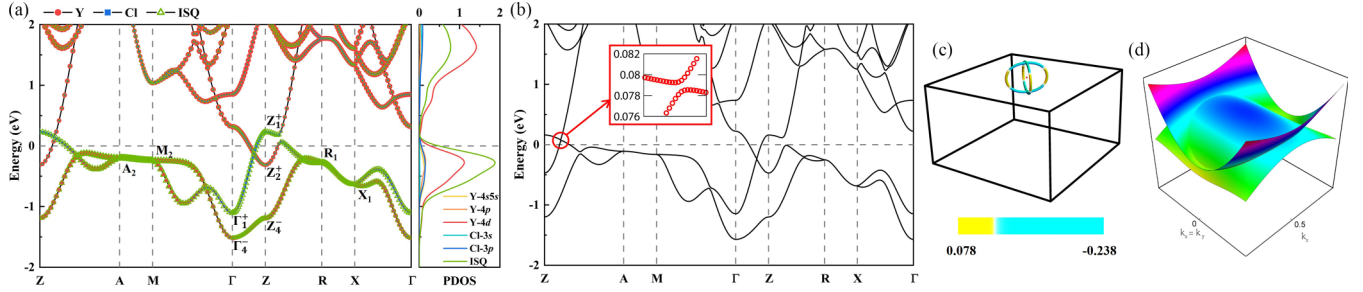
FIG. 4. (a) The orbital-projected band structure and PDOS [states per eV per f.u. (formula unit)] of t-YCl and (b) band with ISQ at 10 GPa. (c) Schematic diagram of the nodal chain in the BZ. (d) The 2D projected band structures of t-YCl system in the $k_x = k_y$ plane near the Z point.

written as follows:

$$H(\vec{k}) = g_0(\vec{k})\tau_0 + g_x(\vec{k})\tau_x + g_z(\vec{k})\tau_z$$
$$g_0(\vec{k}) = M_0 - B_0(k_x^2 + k_y^2) - C_0 k_z^2$$
$$g_x(\vec{k}) = A(k_x^2 - k_y^2)$$
$$g_z(\vec{k}) = M_z - B_z(k_x^2 + k_y^2) - C_z k_z^2. \tag{1}$$

Here, the τ_x and τ_z are Pauli matrices; τ_0 is a 2×2 identity matrix. This system hosts both TRS and inversion symmetry (IS); thus, the component of τ_y must be zero. By diagonalizing the 2×2 effective Hamiltonian, the eigenvalues of the two-level system can be obtained as $E(\vec{k}) = g_0(\vec{k}) \pm \sqrt{g_x^2 + g_z^2}$. When $g_x = g_z = 0$, band crossings occur. It is clear that $g_z(\vec{k}) = 0$ gives us $M_z B_z > 0$ and $M_z C_z > 0$, which is exactly the condition of band inversion, and the corresponding solution is an ellipsoid surrounding the Z point. Furthermore, $g_x(\vec{k}) = 0$ confines the band crossings in the R_{4z}-related $k_x = \pm k_y$ planes. As a result, the solutions of $g_z(\vec{k}) = 0$ and $g_x(\vec{k}) = 0$ are nothing other than intersecting lines between the ellipsoid and the $k_x = \pm k_y$ planes, which gives a nodal chain consisting of two nodal lines located on the $k_x = k_y$ and $k_x = -k_y$ planes, respectively. On the basis of theoretical analysis, 2D band scanning near Z in the $k_x = k_y$ plane between the conduction-band minimum and valence-band maximum is presented in Fig. 4(c); a nodal ring in the $k_x = k_y$ plane can be clearly obtained. Combining the R_{4z}-related nodal line in the $k_x = -k_y$ plane, the nodal chain appears, as shown in Fig. 4(d).

SOC often plays an important role in engineering topological states, such as quantum spin Hall effect in graphene [71,72] and $Ta_2 M_3 Te_5$ (M = Pd, Ni) compounds [73,74], 3D large SOC-gap topological insulator in $Bi_2 Se_3$ and NaCaBi families [75,76], and so on. In terms of the t-YCl system, once SOC is included, this nodal chain disappears, leaving only two R_{4z}-protected Dirac points locating at $(0, 0, \pm k_c)$ with $k_c = 0.3193 \frac{2\pi}{c}$.

Thanks to the recently developed theory of TQC [54], BR has been listed in all space groups [55]. The irreducible representations of the high-symmetry $\boldsymbol{k}$ points are calculated and labeled in Fig. 4(a). Accordingly, BR analysis indicates that the two lowest conduction bands belong to $A1@2a$ BR. Since the Y and Cl atom occupy the 2c Wyckoff positions, i.e., no atoms in t-YCl locates the 2a Wyckoff positions, suggesting the unconventional nature (obstructed) atomic

limit [47,65,77,78]. Based on BR analysis, the ionic t-YCl with the unconventional nature has great potential to be an electride material.

According to the ELF of t-YCl shown in Fig. 5(a), an attractor (non-nuclear maxima in the ELF maps) off the nuclei can be observed in the interlamination at 2a Wyckoff positions. Further, the contours of ELF show that the centers of ELF attractors are very strong, with the value close to 1 [Fig. 5(b)]. This strong aggregation of electrons without nucleus suggests the ISQ's feature. Therefore, t-YCl is a 0D electride with ISQ locating at 2a Wyckoff positions.

To further uncover the influence of ISQs, the band structure, and projected densities of states (PDOS), consider the ISQs are adopted [Fig. 4(a)]. The ISQ curves in band structures and DOSs are calculate by adding pseudoatoms [35,79] with a sphere radius of 1.5 Å to fit the volumes. As shown in Fig. 4(a), the integration of projected density reveals the quantity of electrostatic charge of ISQs is $\sim$2.091 e_2, which mainly come from Y atoms. Further analysis shows that the ISQs are obviously gathering at Fermi surface and make a major contribution to the band inversion, participating in the topological band inversion.

To determine the WF of t-YCl, we consider the (1 0 0), (0 0 1), and (1 1 0) surfaces, and Figs. 5(c) to 5(e) illustrate the WF of each optimized slab at 0 GPa. The results show that the Φ_{WF} of t-YCl in the (1 0 0), (0 0 1), and (1 1 0) planes are 2.724, 3.135, and 2.95 eV, respectively. Therefore, the work function of t-YCl is 2.724 eV, which is a relatively low value compared to those of Y (3.1 eV) [80] and $Sr_5 P_3$ (2.8 eV) [81], $Y_5 Si_3$ (3.5 eV) [38] and $Y_2 C$ (2.84 eV) [79]. This result reveals the loose bound character of delocalized electrons in t-YCl and explains the contribution of ISQs clustered nearby the Fermi level.

For other Y-Cl phases, the calculated ELF is presented in Fig. S2 of Supplemental Material [67]. At corresponding pressure, the significant non-nuclear charge accumulations in $Cmcm$ $Y_2 Cl$, R-$3m$ $Y_3 Cl_2$, $C2/m$ $Y_2 Cl_3$, and $P2_1/m$ YCl_2 indicate their electride feature. Including the R-$3m$ $Y_3 Cl_2$ and $C2/m$ $Y_2 Cl_3$ reported before, the electrides of $Cmcm$ $Y_2 Cl$, t-YCl, and $P2_1/m$ YCl_2 are also stable at around 10 GPa, which proves that the moderate pressure is conducive to the production of electronic compounds in the Y-Cl systems. The electronic structure calculations show the metallic properties of $Cmcm$ and $I4/mcm$ $Y_2 Cl$, R-$3m$ and $P4/mbm$ $Y_3 Cl_2$, $P6_3/mmc$ and $Cmcm$ YCl, $P2_1/m$ and $I4/mmm$ YCl_2 at counterpart pressures. While $C2/m$ $Y_2 Cl_3$, $C2/m$, $Cmcm$, $P2_1/c$, and $Pnma$ YCl_3 exhibit nonmetallic properties, with
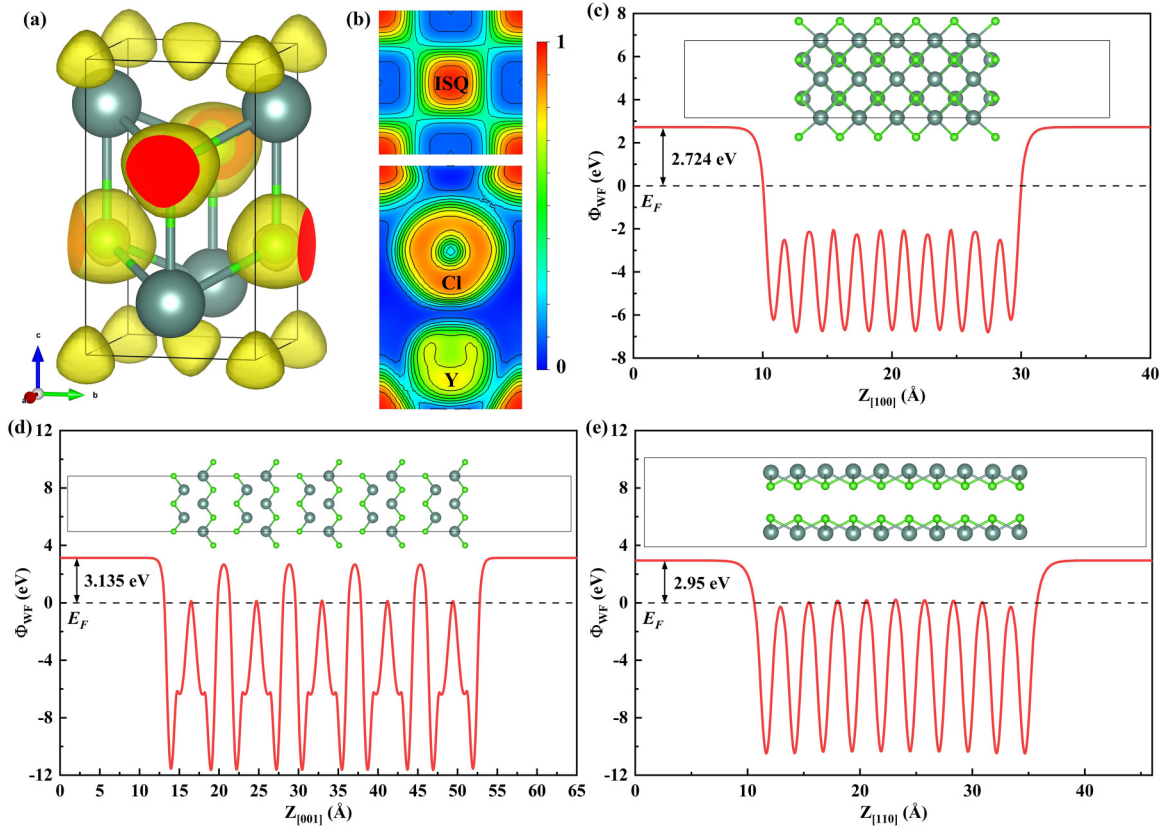
FIG. 5. (a) ELF of t-YCl at 10 GPa with isosurface of 0.8. (b) ELF contours of t-YCl on the (0 0 1) and (1 0 0) planes at 10 GPa; the division adopts linear mode with interval of 0.1. Calculated work functions as a function of position (Å) along c axis for t-YCl in the (c) [100], (d) [001], and (e) [110] crystal planes; the Fermi level is set as 0 eV.

the band gap $\sim$0.754, 4.972, 3.018, 2.875 and 1.177 eV under pressure, respectively (see in Supplemental Material, [67] Fig. S3).

IV. CONCLUSION

In summary, we studied Y-Cl binary system under pressure by crystal-structure prediction, and identified seven structures, including $Cmcm$ Y$_2$Cl, $P4/mbm$ Y$_3$Cl$_2$, $P4/nmm$ YCl, $Cmcm$ YCl, $P2_1/m$ YCl$_2$, $P2_1/c$ YCl$_3$, and $Pnma$ YCl$_3$, in which the $Cmcm$ Y$_2$Cl, t-YCl, $C2/m$ Y$_2$Cl$_3$, and $P2_1/m$ YCl$_2$ phases are found to be electrides. Based on DFT calculations and symmetry analyses, we find that the t-YCl is not only a topological nontrivial material, but also an electride. In addition, calculations of the phonon spectrum and MD indicate that the t-YCl can be obtained at high pressure and annealed to at ambient conditions. Analyses of the topological electronic band structure reveal that the t-YCl is a nodal-chain semimetal without SOC. Once including SOC, this nodal chain disappears, leaving only two R_{4z}-protected Dirac points locating at $(0, 0, \pm k_c)$ with $k_c = 0.3193\frac{2\pi}{c}$. Utilizing the TQC with BR analysis, we find the highest occupied bands belong to $A1@2a$ BR, which indicates the unconventional nature. As expected, the first-principles calculations confirm the existence of an uncompensated state at the $(0,0,0)$ and $(0.5,0.5,0)$ site with no atoms occupying but ISQs there. Through PDOS and projected band analyses, we found that the 0D ISQs in t-YCl with near 2.091 electrons are concentrated near the Fermi level and contributes to the band inversion for the nodal chain. The relatively low WF (2.724 eV) at (1 0 0) surface revealed the loose bound character of delocalized electrons in electride. This result determined that t-YCl is a topological electride whose topological state is mainly contributed by ISQs. We believe that the current work may inspire further theoretical and experimental investigations.

The data that support the findings of this study are available from the corresponding authors upon reasonable request.

[1] X. Wan, A. M. Turner, A. Vishwanath, and S. Y. Savrasov, Topological semimetal and Fermi-arc surface states in the electronic structure of pyrochlore iridates, Phys. Rev. B **83**, 205101 (2011).

[2] Z. Wang, Y. Sun, X.-Q. Chen, C. Franchini, G. Xu, H. Weng, X. Dai, and Z. Fang, Dirac semimetal and topological phase transitions in A_3Bi (A = Na, K, Rb), Phys. Rev. B **85**, 195320 (2012).

[3] Z. Wang, H. Weng, Q. Wu, X. Dai, and Z. Fang, Three-dimensional Dirac semimetal and quantum transport in Cd_3As_2, Phys. Rev. B **88**, 125427 (2013).

[4] N. P. Armitage, E. J. Mele, and A. Vishwanath, Weyl and Dirac semimetals in three-dimensional solids, Rev. Mod. Phys. **90**, 015001 (2018).

[5] H. Weng, C. Fang, Z. Fang, B. A. Bernevig, and X. Dai, Weyl semimetal phase in noncentrosymmetric transition-metal monophosphides, Phys. Rev. X **5**, 011029 (2015).

[6] J. Ruan, S.-K. Jian, H. Yao, H. Zhang, S.-C. Zhang, and D. Xing, Symmetry-protected ideal Weyl semimetal in HgTe-class materials, Nat. Commun. **7**, 11136 (2016).

[7] N. Xu et al., Observation of Weyl nodes and Fermi arcs in tantalum phosphide, Nat. Commun. **7**, 11006 (2016).

[8] B. Q. Lv et al., Observation of Weyl nodes in TaAs, Nat. Phys. **11**, 724 (2015).

[9] J. Liu and D. Vanderbilt, Weyl semimetals from noncentrosymmetric topological insulators, Phys. Rev. B **90**, 155316 (2014).

[10] S.-Y. Xu et al., Discovery of a Weyl fermion semimetal and topological Fermi arcs, Science. **349**, 613 (2015).

[11] S.-Y. Xu et al., Experimental discovery of a topological Weyl semimetal state in TaP, Sci. Adv. **1**, e1501092 (2015).

[12] S.-Y. Xu et al., Discovery of a Weyl fermion state with Fermi arcs in niobium arsenide, Nat. Phys. **11**, 748 (2015).

[13] L. Lu, Z. Wang, D. Ye, L. Ran, L. Fu, J. D. Joannopoulos, and M. Soljačić, Experimental observation of Weyl points, Science. **349**, 622 (2015).

[14] S.-M. Huang et al., A Weyl fermion semimetal with surface Fermi arcs in the transition metal monopnictide TaAs class, Nat. Commun. **6**, 7373 (2015).

[15] B. Q. Lv et al., Experimental discovery of Weyl semimetal TaAs, Phys. Rev. X **5**, 031013 (2015).

[16] S. M. Young, S. Zaheer, J. C. Y. Teo, C. L. Kane, E. J. Mele, and A. M. Rappe, Dirac semimetal in three dimensions, Phys. Rev. Lett. **108**, 140405 (2012).

[17] B.-J. Yang and N. Nagaosa, Classification of stable three-dimensional Dirac semimetals with nontrivial topology, Nat. Commun. **5**, 4898 (2014).

[18] Z. K. Liu et al., A stable three-dimensional topological Dirac semimetal Cd_3As_2, Nat. Mater. **13**, 677 (2014).

[19] Z. K. Liu et al., Discovery of a three-dimensional topological Dirac semimetal, Na_3Bi, Science. **343**, 864 (2014).

[20] M. Neupane et al., Observation of a three-dimensional topological Dirac semimetal phase in high-mobility Cd_3As_2, Nat. Commun. **5**, 3786 (2014).

[21] S.-Y. Xu et al., Observation of Fermi arc surface states in a topological metal, Science. **347**, 294 (2015).

[22] P. Tang, Q. Zhou, G. Xu, and S.-C. Zhang, Dirac fermions in an antiferromagnetic semimetal, Nat. Phys. **12**, 1100 (2016).

[23] C. Fang, Y. Chen, H.-Y. Kee, and L. Fu, Topological nodal line semimetals with and without spin-orbital coupling, Phys. Rev. B **92**, 081201(R) (2015).

[24] R. Yu, Z. Fang, X. Dai, and H. Weng, Topological nodal line semimetals predicted from first-principles calculations, Front. Phys. **12**, 127202 (2017).

[25] C. Fang, H. Weng, X. Dai, and Z. Fang, Topological nodal line semimetals, Chin. Phys. B **25**, 117106 (2016).

[26] Z. Song, T. Zhang, and C. Fang, Diagnosis for nonmagnetic topological semimetals in the absence of spin-orbital coupling, Phys. Rev. X **8**, 031069 (2018).

[27] T. Bzdušek, Q. Wu, A. Rüegg, M. Sigrist, and A. A. Soluyanov, Nodal-chain metals, Nature (London) **538**, 75 (2016).

[28] S.-S. Wang, Y. Liu, Z.-M. Yu, X.-L. Sheng, and S. A. Yang, Hourglass Dirac chain metal in rhenium dioxide, Nat. Commun. **8**, 1844 (2017).

[29] R. Yu, Q. Wu, Z. Fang, and H. Weng, From nodal chain semimetal to Weyl semimetal in HfC, Phys. Rev. Lett. **119**, 036401 (2017).

[30] G. Chang et al., Topological Hopf and chain link semimetal states and their application to Co_2MnGa, Phys. Rev. Lett. **119**, 156401 (2017).

[31] D. Shao and C. Fang, Filling-enforced Dirac nodal loops in nonmagnetic systems and their evolutions under various perturbations, Phys. Rev. B **102**, 165135 (2020).

[32] B. Bradlyn, J. Cano, Z. Wang, M. G. Vergniory, C. Felser, R. J. Cava, and B. A. Bernevig, Beyond Dirac and Weyl fermions: Unconventional quasiparticles in conventional crystals, Science. **353**, aaf5037 (2016).

[33] J. L. Dye, Electrides: Ionic salts with electrons as the anions, Science. **247**, 663 (1990).

[34] M.-S. Miao and R. Hoffmann, High pressure electrides: A predictive chemical and physical theory, Acc. Chem. Res. **47**, 1311 (2014).

[35] M. Miao and R. Hoffmann, High-pressure electrides: The chemical nature of interstitial quasiatoms, J. Am. Chem. Soc. **137**, 3631 (2015).

[36] Y. Toda, S. Matsuishi, K. Hayashi, K. Ueda, T. Kamiya, M. Hirano, and H. Hosono, Field emission of electron anions clathrated in subnanometer-sized cages in $[Ca_{24}Al_{28}O_{64}]^{4+}(4e^-)$, Adv. Mater. **16**, 685 (2004).

[37] S. W. Kim, T. Shimoyama, and H. Hosono, Solvated electrons in high-temperature melts and glasses of the room-temperature stable electride $[Ca_{24}Al_{28}O_{64}]^{4+}$ $4e^-$, Science. **333**, 71 (2011).

[38] Y. Lu, J. Li, T. Tada, Y. Toda, S. Ueda, T. Yokoyama, M. Kitano, and H. Hosono, Water durable electride Y_5Si_3: Electronic structure and catalytic activity for ammonia synthesis, J. Am. Chem. Soc. **138**, 3970 (2016).

[39] Z. Zhao, S. Zhang, T. Yu, H. Xu, A. Bergara, and G. Yang, Predicted pressure-induced superconducting transition in electride Li_6P, Phys. Rev. Lett. **122**, 097002 (2019).

[40] H. Hosono and M. Kitano, Advances in materials and applications of inorganic electrides, Chem. Rev. **121**, 3121 (2021).

[41] Y. Xu, L. Zheng, Y. Zhang, Z. Zhang, Q. Wang, Y. Zhang, L. Chen, C. Fang, B. Wan, and H. Gou, Strong Electron correlation-induced Mott-insulating electrides of Ae_5X_3 (Ae = Ca, Sr, and Ba; X = As and Sb), Matter Radiat. Extrem. **9**, (2024).

[42] D. J. Singh, H. Krakauer, C. Haas, and W. E. Pickett, Theoretical determination that electrons act as anions in the electride Cs^+ (15-Crown-5)$_2 \cdot e^-$, Nature (London) **365**, 39 (1993).

[43] P. V. Sushko, A. L. Shluger, K. Hayashi, M. Hirano, and H. Hosono, Electron localization and a confined electron gas in nanoporous inorganic electrides, Phys. Rev. Lett. **91**, 126401 (2003).

[44] S. Matsuishi, Y. Toda, M. Miyakawa, K. Hayashi, T. Kamiya, M. Hirano, I. Tanaka, and H. Hosono, High-density electron anions in a nanoporous single crystal: $[Ca_{24}Al_{28}O_{64}]^{4+}$ (4e$^-$), Science. **301**, 626 (2003).

[45] Y. Toda, H. Yanagi, E. Ikenaga, J. J. Kim, M. Kobata, S. Ueda, T. Kamiya, M. Hirano, K. Kobayashi, and H. Hosono, Work function of a room-temperature, stable electride $[Ca_{24}Al_{28}O_{64}]^{4+}(e^-)_4$, Adv. Mater. **19**, 3564 (2007).

[46] K. Lee, S. W. Kim, Y. Toda, S. Matsuishi, and H. Hosono, Dicalcium nitride as a two-dimensional electride with an anionic electron layer, Nature (London) **494**, 336 (2013).

[47] S. Nie, Y. Qian, J. Gao, Z. Fang, H. Weng, and Z. Wang, Application of topological quantum chemistry in electrides, Phys. Rev. B **103**, 205133 (2021).

[48] B. Wan *et al.*, Identifying quasi-2D and 1D electrides in yttrium and scandium chlorides via geometrical identification, npj Comput. Mater. **4**, 77 (2018).

[49] L. Jin, X. Zhang, T. He, W. Meng, X. Dai, and G. Liu, Ferromagnetic two-dimensional metal-chlorides MCl (M = Sc, Y, and La): Candidates for Weyl nodal line semimetals with small spin-orbit coupling gaps, Appl. Surf. Sci. **520**, 146376 (2020).

[50] R. J. Hemley, Percy W. Bridgman's second century, High Press. Res. **30**, 581 (2010).

[51] L. Zhang, Y. Wang, J. Lv, and Y. Ma, Materials discovery at high pressures, Nat. Rev. Mater. **2**, 17005 (2017).

[52] Y. Ma, M. Eremets, A. R. Oganov, Y. Xie, I. Trojan, S. Medvedev, A. O. Lyakhov, M. Valle, and V. Prakapenka, Transparent dense sodium, Nature (London) **458**, 182 (2009).

[53] B. Wan, J. Zhang, L. Wu, and H. Gou, High-pressure electrides: From design to synthesis, Chin. Phys. B **28**, 106201 (2019).

[54] B. Bradlyn, L. Elcoro, J. Cano, M. G. Vergniory, Z. Wang, C. Felser, M. I. Aroyo, and B. A. Bernevig, Topological quantum chemistry, Nature (London) **547**, 298 (2017).

[55] J. Cano, B. Bradlyn, Z. Wang, L. Elcoro, M. G. Vergniory, C. Felser, M. I. Aroyo, and B. A. Bernevig, Building blocks of topological quantum chemistry: Elementary band representations, Phys. Rev. B **97**, 035139 (2018).

[56] Y. Wang, J. Lv, L. Zhu, and Y. Ma, Crystal structure prediction via particle-swarm optimization, Phys. Rev. B **82**, 094116 (2010).

[57] Y. Wang, J. Lv, L. Zhu, and Y. Ma, CALYPSO: A method for crystal structure prediction, Comput. Phys. Commun. **183**, 2063 (2012).

[58] K. Xia, H. Gao, C. Liu, J. Yuan, J. Sun, H.-T. Wang, and D. Xing, A novel superhard tungsten nitride predicted by machine-learning accelerated crystal structure search, Sci. Bull. **63**, 817 (2018).

[59] H. Gao, J. Wang, Y. Han, and J. Sun, Enhancing crystal structure prediction by decomposition and evolution schemes based on graph theory, Fundam. Res. **1**, 466 (2021).

[60] J. Wang, H. Gao, Y. Han, C. Ding, S. Pan, Y. Wang, Q. Jia, H.-T. Wang, D. Xing, and J. Sun, MAGUS: Machine learning and graph theory assisted universal structure searcher, Natl. Sci. Rev. **10**, nwad128 (2023).

[61] W. Kohn and L. J. Sham, Self-consistent equations including exchange and correlation effects, Phys. Rev. **140**, A1133 (1965).

[62] J. P. Perdew, K. Burke, and M. Ernzerhof, Generalized gradient approximation made simple, Phys. Rev. Lett. **77**, 3865 (1996).

[63] A. Togo, First-principles phonon calculations with phonopy and Phono3py, J. Phys. Soc. Jpn. **92**, 012001 (2023).

[64] J. Gao, Q. Wu, C. Persson, and Z. Wang, Irvsp: To obtain irreducible representations of electronic states in the VASP, Comput. Phys. Commun. **261**, 107760 (2021).

[65] J. Gao, Y. Qian, H. Jia, Z. Guo, Z. Fang, M. Liu, H. Weng, and Z. Wang, Unconventional materials: The mismatch between electronic charge centers and atomic positions, Sci. Bull. **67**, 598 (2022).

[66] H. Yu and Y. Chen, Pressure-induced electrides and metallic phases in the Y–Cl system, J. Phys.: Condens. Matter **33**, 215401 (2021).

[67] See Supplemental Material at http://link.aps.org/supplemental/10.1103/PhysRevResearch.6.023249 for the details of structural parameters, phonon dispersions, ELF, and band structures of Y-Cl compound.

[68] Y. Yin *et al.*, Synthesis of rare-earth metal compounds through enhanced reactivity of alkali halides at high pressures, Commun. Chem. **5**, 122 (2022).

[69] H. Mattausch, J. B. Hendricks, R. Eger, J. D. Corbett, and A. Simon, Reduced halides of yttrium with strong metal-metal bonding: Yttrium monochloride, monobromide, sesquichloride, and sesquibromide, Inorg. Chem. **19**, 2128 (1980).

[70] D. H. Templeton and G. F. Carter, The crystal structures of yttrium trichloride and similar compounds, J. Phys. Chem. **58**, 940 (1954).

[71] C. L. Kane and E. J. Mele, Z_2 topological order and the quantum spin Hall effect, Phys. Rev. Lett. **95**, 146802 (2005).

[72] C. L. Kane and E. J. Mele, Quantum spin Hall effect in graphene, Phys. Rev. Lett. **95**, 226801 (2005).

[73] Z. Guo, D. Yan, H. Sheng, S. Nie, Y. Shi, and Z. Wang, Quantum spin Hall effect in Ta$_2M_3$Te$_5$ (M = Pd,Ni), Phys. Rev. B **103**, 115145 (2021).

[74] X. Wang *et al.*, Observation of topological edge states in the quantum spin Hall insulator Ta$_2$Pd$_3$Te$_5$, Phys. Rev. B **104**, L241408 (2021).

[75] H. Zhang, C.-X. Liu, X.-L. Qi, X. Dai, Z. Fang, and S.-C. Zhang, Topological insulators in Bi$_2$Se$_3$, Bi$_2$Te$_3$ and Sb$_2$Te$_3$ with a single Dirac cone on the surface, Nat. Phys. **5**, 438 (2009).

[76] D. Shao, Z. Guo, X. Wu, S. Nie, J. Sun, H. Weng, and Z. Wang, Topological insulators in the NaCaBi family with large spin-orbit coupling gaps, Phys. Rev. Res. **3**, 013278 (2021).

[77] S. Nie, B. A. Bernevig, and Z. Wang, Sixfold excitations in electrides, Phys. Rev. Res. **3**, L012028 (2021).

[78] Y. Xu, L. Elcoro, Z.-D. Song, M. G. Vergniory, C. Felser, S. S. P. Parkin, N. Regnault, J. L. Mañes, and B. A. Bernevig, Filling-enforced obstructed atomic insulators, Phys. Rev. B **109**, 165139 (2024).

[79] X. Zhang, Z. Xiao, H. Lei, Y. Toda, S. Matsuishi, T. Kamiya, S. Ueda, and H. Hosono, Two-dimensional transition-metal electride Y$_2$C, Chem. Mater. **46**, 6638 (2014).

[80] D. E. Eastman, Photoelectric work functions of transition, rare-earth, and noble metals, Phys. Rev. B **2**, 1 (1970).

[81] J. Wang, K. Hanzawa, H. Hiramatsu, J. Kim, N. Umezawa, K. Iwanaka, T. Tada, and H. Hosono, Exploration of stable strontium phosphide-based electrides: Theoretical structure prediction and experimental validation, J. Am. Chem. Soc. **139**, 15668 (2017).

Correction: A sign error in Eq. (1) has been fixed. The caption to Fig. 1 contained a typographical error and has been fixed.